Aerospace Science and Technology 87 (2019) 73–88

Contents lists available at ScienceDirect

Aerospace Science and Technology

www.elsevier.com/locate/aescte

Investigation of a sliding alula for control augmentation of lifting surfaces at high angles of attack

Thomas Linehan [a], Kamran Mohseni [b,*]

[a] Department of Mechanical & Aerospace Engineering, University of Florida, Gainesville, FL, 32611, United States of America
[b] Department of Mechanical & Aerospace Engineering and Department of Electrical and Computer Engineering, University of Florida, Gainesville, FL, 32611, United States of America

ARTICLE INFO

Article history:
Received 28 November 2018
Received in revised form 3 February 2019
Accepted 4 February 2019
Available online 8 February 2019

ABSTRACT

The ability to generate useful control forces on lifting surfaces at high angles of attack is particularly challenging due to boundary layer separation. A miniature collection of feathers on birds termed the alula, appears an intriguing solution to this control problem. Using surface-oil visualizations and direct force and moment measurements, we experimentally investigate the aerodynamics of a model alula(e) affixed to a thin, flat-plate, $\mathcal{AR} = 1.5$ rectangular wing. A critical parameter of the deflected alula considered, is not its orientation relative to the incoming flow, but rather its spanwise distance from the wing tip to which it is oriented. Control forces (lift and rolling moment) are proportional to this distance over a wide range of angles of attack. When centered on the stalled wing, a single alula generates a rolling moment of magnitude comparable to that produced by a conventional trailing-edge flap aileron in an attached-flow condition. Importantly, the wetted area of the alula is one order of magnitude less than the reference flap aileron. The uncharacteristically large control force of the alula stems from its ability to induce and stabilize a vortex that sweeps outboard across the span of the wing towards the wing tip. Changing the distance of the alula from the wing tip, varies the length of this 'sweeping vortex' and its associated interactions with the wing. A novel high-angle-of-attack control solution is proposed, the sliding alula, which entails coordinated shifting of two alulae to manipulate the length and asymmetry of stabilized 'sweeping vortices' on stalled wings. Results regarding control authority in cross-flow and the gust mitigation potential of the sliding alula are also discussed.

Published by Elsevier Masson SAS.

1. Introduction

A wide variety of applications ranging from underwater vehicles to aircraft require the ability to maneuver at low speeds in all or portions of their operating envelope. Applications with stringent cost, size, weight, and power constraints tend to rely on controlling the forces and moments produced by lifting surfaces operating at high angles of attack, for example the wings of an unmanned aerial vehicle (UAV) during landing, rather than alternate solutions such as thrust vectoring.

Generating useful control forces on lifting surfaces at high angles of attack is particularly challenging due to boundary layer separation. Under these conditions, stalled flow over improperly placed control surfaces diminishes their control authority. Figure 1 depicts this trend. Here, roll moment coefficient measurements produced by a $-20°$ aileron-flap deflection are plotted as a function of angle of attack for rectangular wings of varying aspect ratio. The Reynolds number for these experiments was $Re = O(10^6)$ where data was redigitized from Fischel et al. [1]. The arrows mark the approximate angle of attack of maximum lift as an indicator of lift stall. For the $\mathcal{AR} = 2.13$ and $\mathcal{AR} = 4.13$ wings, a precipitous loss in control power follows lift stall as expected for a control surface placed at the trailing-edge of a stalled wing. This trend would hinder the aircraft's ability to both trim and maneuver at high angles of attack limiting its operational flight envelope.

In light of this challenge, research into novel control strategies has drawn increased attention [2–5]. Jones et al. [6] conducted static experiments on an airfoil with a leading-edge flap. The authors suggest that the leading-edge flap acts as a transition-trip device granting higher maximum lift than a traditional surface-mounted trip. Other research has attempted to control the development, stabilization, and convection of leading-edge vortices (LEVs) [7–9]. The numerical computations of Drost et al. [7] indicate that high frequency actuation of a hinged, deflected leading-edge flap elicits $> 50\%$ increase in lift-to-drag-ratio compared to a 27% increase in the static deflected case. An additional benefit of leading-edge control surfaces is the ability to leverage the

* Corresponding author.
E-mail address: mohseni@ufl.edu (K. Mohseni).

https://doi.org/10.1016/j.ast.2019.02.008
1270-9638/Published by Elsevier Masson SAS.

Nomenclature

Re	Reynolds number based on root chord
q	dynamic pressure
ρ	density of air
b	wingspan
c	wing chord
S	wing area
$\mathcal{AR}$	aspect ratio, $\frac{b^2}{S}$
U_∞	freestream velocity
C_L	lift coefficient, $\frac{2L}{\rho U_\infty^2 S}$
C_D	drag coefficient, $\frac{2D}{\rho U_\infty^2 S}$
C_M	quarter-chord pitching moment coefficient, $\frac{2M}{\rho U_\infty^2 Sc}$
C_l	roll moment coefficient, $\frac{2l}{\rho U_\infty^2 Sb}$
α	angle of attack ..... deg.
β	sideslip angle ..... deg.
y	spanwise position of the alula root relative to the midspan of the wing
d	distance of the alula root from the left wing tip
ϕ	alula deflection angle
γ	alula incidence angle
LO	leftward oriented
RO	rightward oriented
LEO	leeward oriented
WO	windward oriented

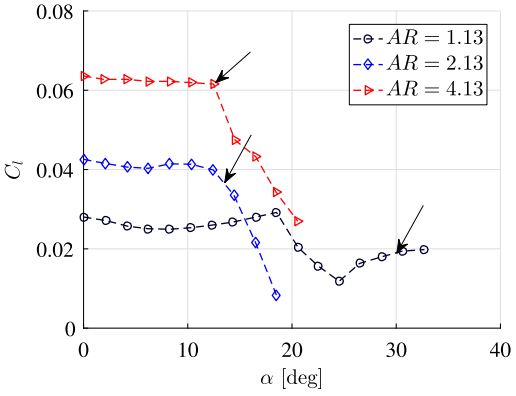

Fig. 1. Reduction of roll moment at high angles of attack as produced by a $-20°$ aileron flap deflection on rectangular wings of varying aspect ratio. Arrows mark the angle of attack of maximum lift as an indicator of lift stall. Reynolds number $O(10^6)$. Data re-digitized from Fischel et al. [1].

pressure peak for actuation which can reduce actuator power consumption [9].

The control problem associated with boundary layer separation becomes further complicated for lifting surfaces of low aspect ratio which exhibit a spanwise variation in separated flow across the wing. For example, moderate to highly-swept wings may display a coexistence of coherent leading-edge vortices, vortex breakdown, and completely stalled flow at a given operating condition [10]. Similar trends were shown on rectangular platforms due to the nonuniform development of the leading-edge vortex across the span of low-aspect-ratio wings [11]. The latter trend likely drives the trailing-edge flap aileron on the $\mathcal{AR} = 1.13$ wing in Fig. 1 to experience a reduction in control force at an angle of attack of increasing lift; an angle of attack well *before* that of lift stall. Similar trends were shown for aileron flaps on an $\mathcal{AR} = 1$ wing at lower Reynolds numbers, $Re = O(10^4)$ [12], suggesting some insensitivity to Reynolds number with regard to this trend.

For applications requiring controlling forces and moments of lifting surfaces of low-aspect-ratio experiencing boundary layer separation, the question is no longer simply what is the proper actuator to influence separated flows, but where does one place such an actuator. Proposed control solutions tend to leverage the fact that low-aspect-ratio lifting surfaces harbor stabilized vortices at high angles of attack, for example the leading-edge vortices of delta wings and the wing-tip vortices of wings of low taper. Hu et al. [13] used passive bleed near the wing tip to manipulate the coherency of the wing-tip vortex and O'Donnell and Mohseni [12] used articulated winglets to manipulate the position of the wing-tip vortex. As operation at high angles of attack is usually a small subset of the operational envelope of a lifting surface, an ideal actuator is one that maximizes control authority during design conditions and minimizes intrusiveness during off-design conditions while being conscious of weight, power, and actuation constraints.

Nature appears to have found one solution to this control problem in the alula; a miniature collection of feathers, 10–15% of the semispan of bird wings, located near the wrist joint at the leading edge of the bird's main wing. During flight at low speeds the alula is observed deflected up from the plane of the wing as shown in Fig. 2. In this deflected state, the alula is recognized as a high-lift device [14–19].

Historically, the proposed aerodynamic mechanisms of the alula have been hypothetical rather than empirical. The gap between the alula and the wing surface has led to connections to be drawn between the alula and a leading-edge slat [15,18,20]; the latter prevents stall by energizing the boundary layer near the leading edge of the wing. However, the alula is canted from the plane of the wing and spans only small percentage of the wing, features

Fig. 2. The left two figures depict a kestrel 'hovering' in a strong headwind. Adapted from Feathered Photography, by Ron Dudley, 2019, retrieved from https://www.featheredphotography.com/blog/2013/03/23/the-alula-bastard-wing-of-a-kestrel-in-flight/. Copyright 2019 Ron Dudley. The right figure depicts a bald eagle maneuvering for landing. Adapted from BR Images Photography, by Beverley Lu, 2019, retrieved from https://www.brimages.ca/blog/birds/bald-eagle-showing-the-alula-in-action. Copyright 2019 Beverley Lu & Roger Herrett. The alula is marked.

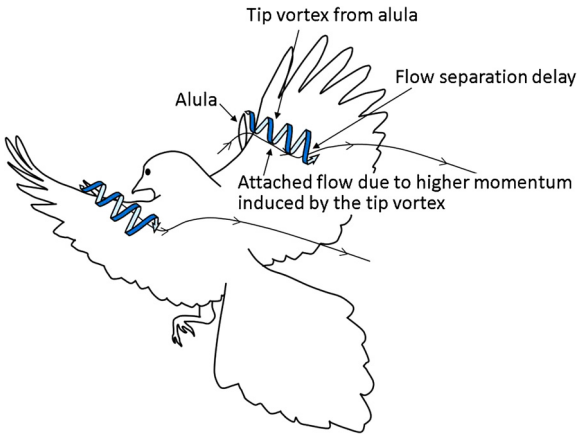

Fig. 3. A depiction of the alula vortex. From Lee et al. [14].

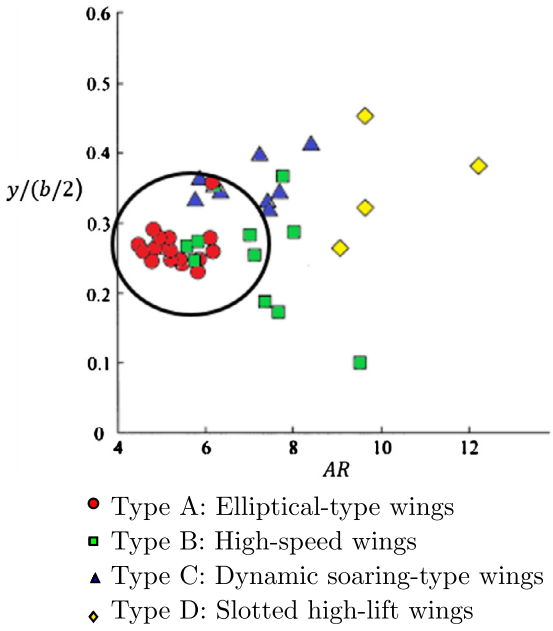

Fig. 4. Measurements of alula location on birds differentiated by wing type. y is the spanwise coordinate whose origin is at the wing root. Re-digitized from [15].

that distinguish it from conventional leading-edge slats. Videler, in his 2005 book [16], proposed two alternative mechanisms: 1. that the alula induces a leading-edge vortex over the hand-wing (region of the wing between the wrist joint and the wing tip) and 2. that the alula generates a small vortex in a similar manner to that produced by a leading-edge fence or sawtooth which separates the attached-flow system on the arm-wing (region of the wing between the wing root and the wrist joint) and the leading-edge vortex on the hand wing. Videler cautions that, 'The reader should be aware that there is no real proof yet for the ideas regarding the function of the alula...'.

In recent work, Lee et al. [14] conducted force and PIV experiments on severed adult-male magpie wings to shed light on the aerodynamic function of the alula. A streamwise vortex stemming from the deployed alula was measured which suggests the aerodynamic function of the alula is more closely aligned with that of a vortex generator. Figure 3 displays an artists rendition of the alula vortex from Lee et al. [14]. The alula vortex imparts strong downwash near the wing surface which decreases the shear-layer thickness and suppresses flow separation over the no deflection case. The authors show that flow separation suppression is more pronounced on the hand-wing than the arm-wing due to the rotation of the alula vortex which introduces additional spanwise flow from the wing root toward the wing tip. While the depiction of the alula as a vortex generator is enticing, in this work we will provide evidence that the control force of the alula stems not from the vortex that it generates but rather the vortex that it induces due to the interaction of the wing flow and the alula at the alula's root.

Few investigators have analyzed the alula from an engineering standpoint. Mandadzhiev et al. [21] investigated the effects of an alula device on a S1223 airfoil for potential use for UAV applications. The parameters investigated were the alula deflection angle, and the alula angle of attack (measured relative to the chord of the wing), where force data and hot-wire anemometry was taken at three angles of attack, $\alpha = 4°, 10°, 18°$, representing pre-stall, stall and post-stall conditions, respectively, at two different Reynolds numbers (Re = 100,000 and 135,000). For the alula parameters tested, lift enhancement was mostly isolated to post-stall angles of attack where increased alula deflection angles in the range $\phi = 4°$–$22°$ increased the magnitude of lift enhancement. From their data the maximum lift enhancement achieved was around 10%. Meseguer et al. [20] investigated a cantilevered wing model affixed with an alula whose geometry and airfoil simulating that of a pidgeon wing. The streamwise location of the alula, nondimensional chord length of the alula, and the nondimensional deflected height of the alula tip was varied. A maximum 22% increase in lift was achieved with the alula with the largest chord length placed coincident with the leading edge of the wing and deflected a height of $0.143l$ off the wing plane, where l is the alula length.

Despite this work, the alula on a finite wing has yet to be explored. Moreover, a potentially critical parameter of the alula was not investigated, its spanwise position, which may have the ability to control the interactions of the alula-induced flow and the wing tip vortex. There exists evidence in nature suggesting the importance of the spanwise position of the alula, at least for certain types of birds. Measurements, of Alvarez et al. [15] on over 40 species of bird wings show a convergence of the spanwise position of the alula, Fig. 4, specifically for birds with Type A: Elliptical-type wings, where the spanwise position of the root of the alula lies in the range $y/(b/2) = 0.25$–0.35, y being the spanwise coordinate measured outboard from the root of the bird wing. Birds categorized with Type A wings by Alvarez et al. have elliptical planforms of low aspect ratio and are active flappers that operate in dense, congested areas and frequently take off and land. These birds would have the most to gain from maximizing the performance of high-lift devices such as the alula and thus it is intriguing to think that the convergence of the spanwise position of their alula is aerodynamically driven.

In this work, we experimentally investigate the aerodynamics of a model alula in an attempt to gauge the alula as a lightweight, minimally intrusive, high-angle-of-attack control solution. Particular attention is made to the spanwise position of the alula, however, several orientational and geometrical parameters are also considered.

The manuscript is organized as follows. The experiment design and methods are described in Section 2. Results regarding the effect of angle of attack, spanwise location, span length, and alula orientation are discussed in Section 3. Here, we show that changing the spanwise location of the alula enables a variable control force over a wide range of angles of attack; a feature not seen when varying the other alula parameters. These results prompt Section 4 which introduces the concept of a sliding alula and presents preliminary experiments judging the control effectiveness of the sliding alula in sideslip. Conclusions are then given in Section 5.

2. Experimental methods

All experiments were conducted in the Engineering Laboratory Design recirculating wind tunnel located at the University of Florida. The test section has a 61×61 cm^2 cross-section and is 2.44 m in length. The wind tunnel can achieve freestream velocities ranging from 3–91.4 m/s and has a freestream turbulence intensity of 0.12% at the tested speeds. Direct six-component force and moment measurements were conducted in the ELD tunnel. The Reynolds number was fixed at 75,000. The details of the models and experiment are described next.

2.1. Wing model

A thin, rectangular, $\mathcal{AR} = 1.5$ wing is chosen as the baseline wing. The aspect-ratio was selected to be similar to those commonly found on experimental fixed-wing Micro-Aerial Vehicles (e.g. Black Widow, NRL MITE2, etc.); aircraft with the most to gain from miniaturized control solutions such as this. Moreover, the $\mathcal{AR} = 1.5$ wing bridges the gap between two types of thin rectangular wings: those of low aspect ratio $\mathcal{AR} < 1.5$ for which the proximity of the tip vortices is sufficient to stabilize the leading-edge vortex and delay stall to high angles of attack, and those of higher aspect ratio $\mathcal{AR} > 1.5$ that do not possess this vortex stabilization ability, leaving stall to occur at low angles of attack. The $\mathcal{AR} = 1.5$ wing exhibits characteristics of both wings in its ability to sustain flow reattachment to a modest angle of attack until an abrupt stall (see Fig. 7). This characteristic enables us to decipher the performance of the alula when the flow over the wing is separated and reattached and the performance of the alula when the wing is massively separated.

The model wing is kept rectangular with a 12.7 cm chord and 17.78 cm span with a thickness-to-chord ratio of 3.5%. A 5:1 elliptical profile was used for the leading edge where the side and trailing edges were left square.

The wing was 3D printed using a 3D Systems Projet 2500 multijet printer. The printer has a net build volume (XYZ) of $294 \times 211 \times 144$ mm with a $800 \times 900 \times 790$ DPI resolution with 32 µm layers. Resolution before post processing is ±0.025–0.05 mm per 25.4 mm of part dimension. The material was VisiJet M2 RWT. Hand finishing (220 grit followed by 600 grit wet sand) was necessary to smooth out the leading edge of the wing.

The wing was designed with seven equally spaced cylindrical housings spread across the leading edge of the wing (see CAD schematic Fig. 5). The housings were designed to accept and secure 3D printed alula attachments or plug inserts. The plug inserts were fabricated to ensure, to machine tolerance, a smooth leading-edge profile. The alula attachments consisted of a plug insert with a fused lifting surface. This lifting surface is modeled as a rigid, rectangular flat plate with a specific orientation with respect to the wing. Details of the parameters of the model alula are described next.

2.2. Parameters of the model alula

The alula is represented as a rigid flat plate with a fixed geometry, orientation, and spanwise position on the wing. The geometry of the alula is described by the span ratio, l/b, or the ratio of the length of the alula to the span of the wing, and its chord ratio, a/c, or the ratio of the alula chord to the chord of the wing. The chord ratio for the alula on the wing was fixed at $a/c = 0.075$ while the span ratio was varied from $l/b = 0.05$ to 0.15. The resulting area of the alula was $A_a = 0.004S$ to $A_a = 0.011S$ The span ratios tested in this investigation are partially motivated by the bird wing measurements of Alvarez et al. [15] which show that the span ratio of the alula ranges from $l/b = 0.5$ (for high speed soaring type birds) to 0.1 (for birds with an elliptical wing with active flapping flight in cluttered environments).

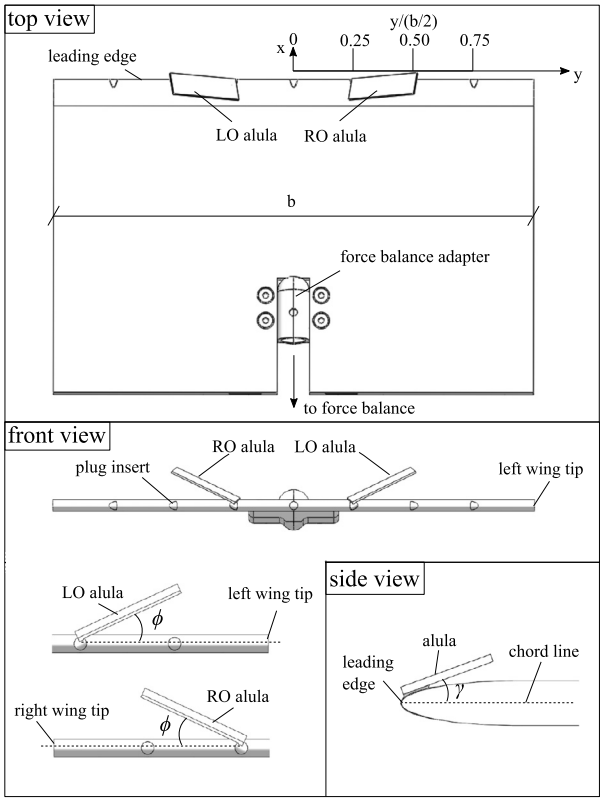

Fig. 5. CAD model of the wing-alula assembly and associated definitions.

The orientation of the deployed alula is defined by three angles: 1. The incidence angle, γ, defined by the angle of the alula chord relative to the wing chord. 2. The deflection angle or cant angle, ϕ, defined by the rotation of the alula from the plane of the wing. 3. The pronation angle, or the sweep angle of the alula (in the plane of the wing) relative to the wing's leading edge. Only the incidence angle and deflection angle are varied in this study. The pronation angle was fixed at 0° such that the leading edge of the alula is aligned with the leading edge of the wing.

The terminology LO and RO is used to designate whether the alula is leftward or rightward oriented, respectively, as seen by an observer at the trailing-edge of the wing facing the leading edge of the wing (see Fig. 5). Unless otherwise noted, the LO alulae are placed on the left semispan of the wing where RO alulae are placed on the right semispan of the wing. Experiments were conducted with the wing affixed with both a single alula and dual alulae. For dual alulae experiments the alula are placed symmetrically about the midspan such that the left and right semispan of the wing are mirror images of each other.

2.3. Force measurements

Aerodynamic forces and moments were measured using the Micro-Loading Technologies (MLT) six-component internal force balance which has been used extensively by our research group [11,22–26]. Each model was swept through angles of attack $\alpha = -10$–46°, in 2° increments using a custom robotic positioning system [27] with a positioning error of ±0.2°. Upon movement to the next angle of attack location, data acquisition was halted for 4 seconds to allow for initial flow transients to subside. Data was then sampled for 5 seconds at 4096 Hz. An identical sweep was made before hand with the wind off which acted as an inertial "tare" set. Strain-gage wind-on data was first subtracted from tare

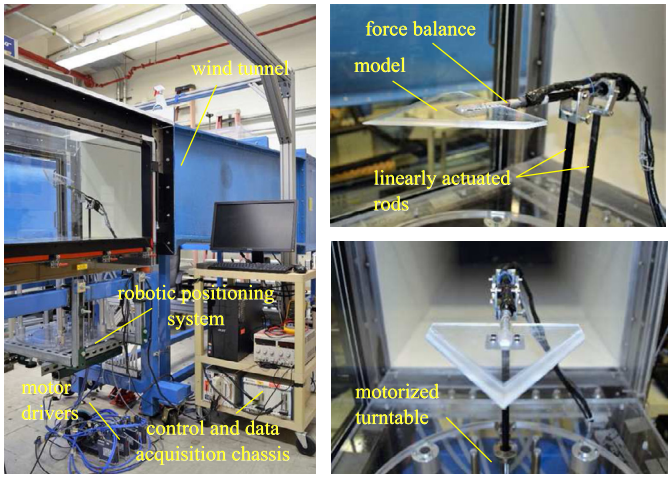

Fig. 6. Experimental facility for force and moment recovery in the ELD wind tunnel. Equipment consists of a four-degree-of-freedom robotic positioning system and a six-component strain-gauge force balance.

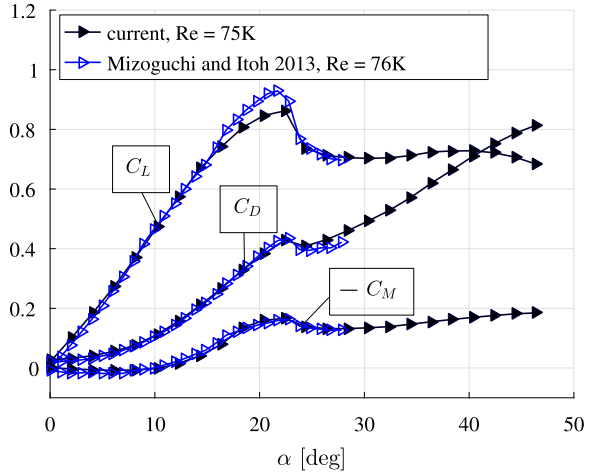

Fig. 7. Validation plot comparing the lift, drag, and nose-down pitching moment coefficient curves of the $\mathcal{AR} = 1.5$ rectangular baseline wing compared to previously published results.

data to isolate the aerodynamic loads from the average inertial loads. Tared strain-gage data was then converted to aerodynamic loads using techniques outlined by the AIAA strain-gauge standard. Blockage effects from streamline curvature, wake, and solid bodies were corrected for based on methods presented by Rae and Pope [28]. Figure 6 depicts the positioning and measurement equipment in the ELD wind tunnel.

The aerodynamic quantities of interest in this paper are the lift coefficient, $C_L = \frac{2L}{\rho U_\infty^2 S}$, drag coefficient, $C_D = \frac{2D}{\rho U_\infty^2 S}$, pitching moment coefficient, $C_M = \frac{2M}{\rho U_\infty^2 Sc}$ (taken about the quarter-chord), and roll moment coefficient, $C_l = \frac{2l}{\rho U_\infty^2 Sb}$. U_∞ is the freestream velocity, ρ is the fluid density, S is the wing area, and b is the wingspan. Estimates of uncertainty for coefficient quantities were obtained by applying the Taylor series method for uncertainty propagation as described in Coleman and Steele [29] to an example test case. The test case was the $\mathcal{AR} = 1.5$ wing at $\alpha = 28°$ with a LO alula of spanlength $l = 0.15b$ ($A_a = 0.011S$) located at $y/(b/2) = 0$ with $\phi = 25°$ and $\gamma = 20°$ subject to uniform fluid with velocity $U_\infty = 9.09$ m/s and fluid density, $\rho = 1.194$ kg/m^3. The measured lift force, L, drag force, D, pitching moment, M, and roll moment, l, at this condition was 0.969 N, 0.604 N, −0.159 N-cm, and 0.056 N-cm. The blockage ratio is approximately 3.0%. Due to the large number of samples, only uncertainties associated with bias errors were considered in this analysis. The absolute bias errors of measured variables, U_∞, b, and c are 0.1 m/s, 0.79 mm, and 0.79 mm, respectively. The relative bias errors of forces and moments are less than 2.3% and 4.2%, respectively. These values constitute the maximum bias error of a set of five repeated known-load experiments with magnitudes comparable to the loads measured in the current study. The relative and absolute (in parenthesis) uncertainties for lift, drag, pitching moment, and roll moment coefficient are computed to be 3.3% ($\Delta C_L = 0.0268$), 4.4% ($\Delta C_D = 0.0223$), 4.9% ($\Delta C_M = 0.0062$), and 4.9% ($\Delta C_l = 0.0015$), respectively.

Figure 7 plots lift, drag, and pitching moment coefficient as a function of angle of attack for the plain $\mathcal{AR} = 1.5$ rectangular wing used in this study (Reynolds number 7.5×10^4) in comparison to re-digitized data from Mizoguchi and Itoh [30] on an $\mathcal{AR} = 1.5$ flat-plate rectangular wing at a similar Reynolds number (Reynolds number 7.6×10^4). The wing model of Mizoguchi and Itoh had a thickness-to-chord ratio of 3.3% (compare to 3.5% for the current wing) with a rounded leading edge and square trailing edge. Good agreement is seen between experiments except for a modest discrepancy in the measured lift peaks between experiments.

Due to the similarity of the wings and Reynolds numbers considered, subsequent experiments were conducted to elucidate the discrepancy in lift between test cases. It was determined that the observed differences in lift at angles of attack near stall are the result of the different wing mounting strategies of the experiments compared i.e. mounting below the wing, as in the Mizoguchi and Itoh study, and mounting in-line with wing, as in the current study.

Figure 8 compares surface-oil flow visualizations with the wing mounted in-line with (top row) and below the wing (bottom row) at several angles of attack. At $\alpha = 20°$, curious dual-lobed oil patterns are observed in the surface-oil visualizations. We attribute these patterns to the presence of an arch-type vortex of similar nature to that which was discovered in computations and subsequent experiments on heaving wings [31,32] and pitching wings [33] of $\mathcal{AR} = 2$ (see Fig. 9). The legs of the arch vortex induce large-scale swirling and a concentric region of low pressure on the wing surface [33], the former which is consistent with observations of the flow development of the current experiment. The existence of the arch-type vortex at angles of attack near that of maximum lift and the subsequent loss of lift that accompanies the loss of this structure, suggest that the arch-type vortex is responsible for the distinct lift peak of this wing. Mounting inline with the wing disrupts the surface flow associated with the arch-type vortex which would reduce the measured lift at this angle of attack. The discrepancies in the surface patterns between the different wing mounting strategies diminish at the higher angles of attack as the flow over the wing becomes massively separated.

2.4. Surface-oil flow visualizations

Surface-oil flow visualizations were conducted to assist in interpreting the aerodynamic mechanisms of the alula. The top surface of the wing was spray-painted white leaving a smooth top surface for oil-pigment transport. The oil-pigment mixture consisted of paraffin oil and commercially available fluorescent pigment (Art 'N Glow pigment powder, particle size 30–50 μm). The following procedure was employed: First, a heavily saturated pigment-oil mixture was applied to the wing at zero pitch angle using a finely bristled brush. The saturated layer was then tipped off with a coarse bristled brush that is wetted with pure paraffin oil. This step ensures an even coating of pigment on the wing and provides a thick layer of oil to facilitate pigment transport. Next, the MPS is commanded to the desired pitch angle and the tunnel velocity is rapidly ramped up to the prescribed freestream velocity. After

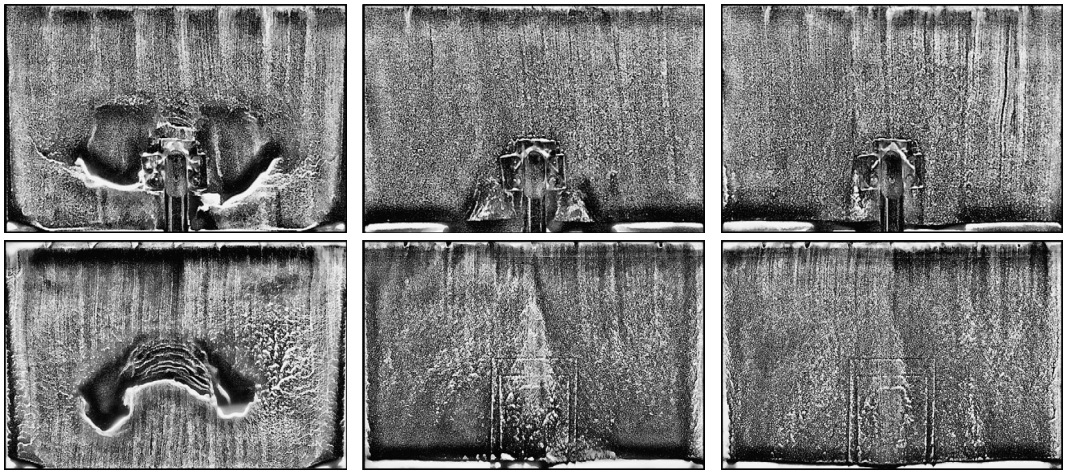

Fig. 8. Effect of the wing mount on the near surface flow. (Top row) Sting mounted inline with the wing. (Bottom row) Sting mounted below the wing. Flow is from top to bottom.

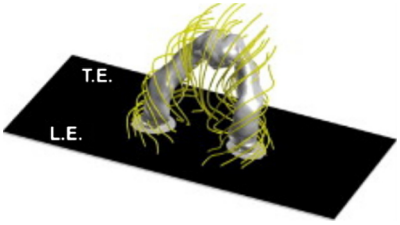

Fig. 9. Arch-type vortex from [31].

>5 min of run time, the pigment is charged using a UV flashlight and the wing is imaged at inclination with the tunnel still running. Lastly, images are dewarped, cropped, and converted into grayscale. Example pre- and post-processed images are shown in Fig. 10 with alulae marked.

3. Results

3.1. Effect of angle of attack

We begin by assessing the control effectiveness of the alula across a wide range of angles of attack. Both a single- and dual-alula configuration is considered. The main focus in this section is on general trends of aerodynamic loads. A more quantitative analysis is given in later sections.

Figure 11 compares the effect of angle of attack on lift, drag, pitching, and roll moment coefficients of the wing affixed with a single alula or dual alulae relative to the plain baseline wing. The top left figure plots lift coefficient, C_L, and ten times the rolling moment coefficient, $10C_l$, whereas the top right figure plots the negative of the quarter-chord pitching moment coefficient, $-C_M$, and the drag coefficient, C_D, each as indicated. With respect to the $-C_M$ curve, increases along the y-axis correspond to an increase in a nose-down pitching moment.

For the single alula case, the alula is placed on the left semispan of the wing with its hinge located at $y/(b/2) = -0.25$. This alula configuration is mirrored on the right side of the wing for the dual-alula case, i.e. $|y/(b/2)| = 0.25$. Each alula is rotated/deflected $\phi = 25°$ from the wing plane as measured clockwise (counterclockwise) for the left (right) alula from an observer located at the trailing-edge of the wing facing the leading edge of the wing. The length (area) and inclination angle of each alula are fixed at $l = 0.15b$ ($A_a = 0.011S$) and $\gamma = 20°$, respectively.

The dominant aerodynamic effects of the alula are isolated to a distinct angle of attack range, $16° < \alpha < 38°$. Throughout this angle of attack range, the wing affixed with a single LO alula placed on the left semispan of the wing generates a positive roll moment. The change in rolling moment is not correlated with changes in the longitudinal loads. For example, at prestall angles of attack within this angle of attack range, $16° < \alpha < 22°$, the nonzero roll moment is accompanied by the reduction in lift, drag, and nose-down pitching moment over the baseline wing. In contrast, at post-stall angles of attack within the range $22° < \alpha < 38°$, the roll moment is accompanied by an increase in lift, drag, and only minor change in nose-down pitching moment over the baseline wing. With regard to the dual-alula case, changes in longitudinal loads relative

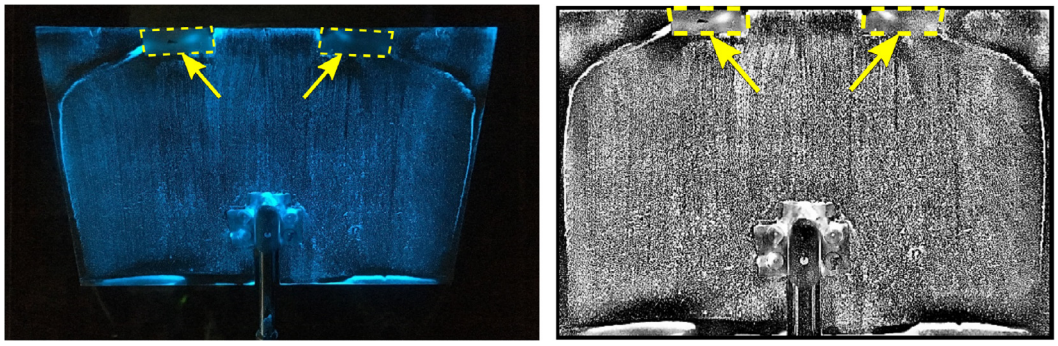

(a) raw image (b) processed image

Fig. 10. Surface-oil flow visualizations before and after being dewarped, cropped, and converted to grayscale. $\alpha = 25°$. Alulae as marked. Flow is top to bottom.

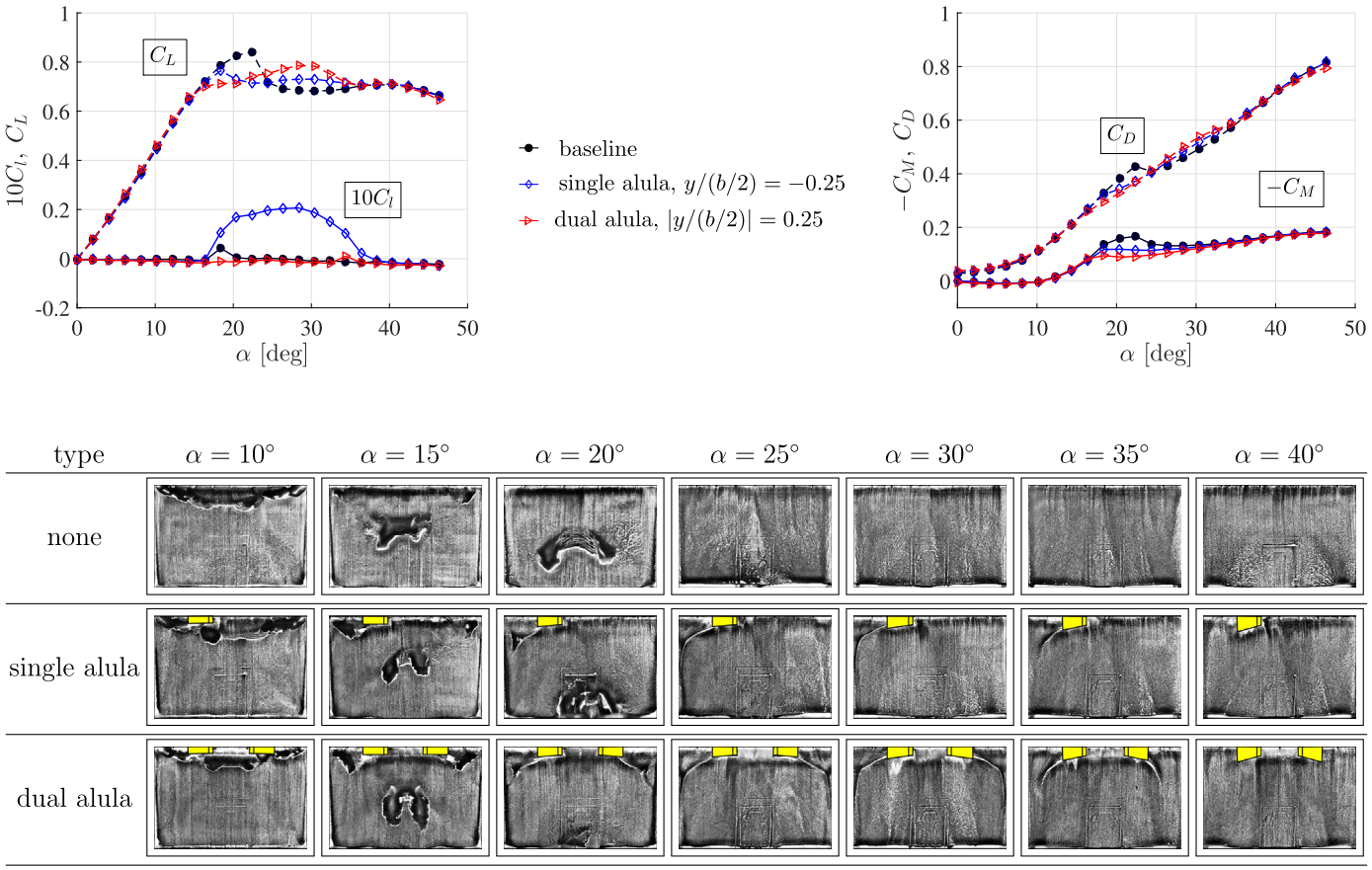

Fig. 11. Comparisons of lift, drag, roll moment, and nose-down pitching moment coefficient curves (top) and surface-oil flow visualizations (bottom) of $\mathcal{AR} = 1.5$ rectangular wing with no alula, single alula, and dual alula at select angles of attack. Flow is from top to bottom.

to the baseline wing follow trends depicted by that of the single alula case. However, increments in the longitudinal loads are generally larger for the dual-alula case. Due to the symmetric alulae configuration, rolling moment remains nominally zero for the dual-alula case.

Notice, that the addition of either a single alula or dual alulae flattens the initial peak of the lift and pitching moment coefficient curves of the baseline wing. This result suggests that an errant deployment of the alula at prestall angles of attack can not only decrease the lift of the wing but would also shift the aerodynamic center of the wing forward which is destabilizing in terms of static pitch stability. The loss of lift associated with the wing-alula combination considered in this study is consistent with previous reports that the alula does not always contribute to lift enhancement [18].

While dominant aerodynamic effects associated with the alula occur at high angles of attack, there exists a performance penalty of operating with a deflected alula at very low angles of attack. For example, the addition of a single alula and dual alulae increases C_{D_0} of the wing by 0.0058 ($\approx 21\%$) and 0.0098 ($\approx 36\%$), respectively. The drag penalty can likely be reduced by storing the alula flush to the wing in off-design flight conditions.

Surface-oil visualizations were conducted at select angles of attack to assist in interpreting trends in aerodynamic loads (bottom of Fig. 11). For these visualizations, the replica sting balance was attached to the wing from below to facilitate visualizations of the surface patterns on the top of the wing.

The surface patterns on the plain wing are analyzed first. At $\alpha = 10°$, a separation bubble spanning the width of the wing is evinced near the wing's leading edge. By $\alpha = 15°$, remnants of the separation bubble remain near the wing tips but can no longer be resolved near the midspan of the wing. A distinct isolated dual lobed surface pattern exists near the center of the wing for which counter-rotating swirling motions occur in each lobe. This structure was previously attributed to the presence of an arch-type vortex and the cause of sustained lift at this angle of attack (recall Fig. 9 and accompanying discussion). At $\alpha = 20°$, an angle of attack near that of maximum lift, the dual lobed surface pattern has shifted aft and grown in spacial extent. By $\alpha = 25°$, this pattern is lost and lift and nose-down pitching moment curves have stalled. At $\alpha \geq 25°$, no clear surface patterns exist on the wing which suggests that the flow over the wing at these angles of attack is massively separated.

Attention is now turned to the surface patterns on wings affixed with both a single and dual alula. At $\alpha = 20°$, the surface patterns for both alula cases depict the clear elimination and/or distortion of the surface pattern attributed to the arch-type vortex on the plain wing. The elimination and/or distortion of this high-lift structure is consistent with the reduction in lift, drag, and pitching moment associated with the presence of the alula at this angle of attack. In addition, beginning at $\alpha = 15°$, curious surface-oil patterns are observed near the upstream corners of the wing at spanwise stations between the alula root and the wing tip. Specifically, distinct separation lines sweep from the alula root toward the wing tip in a manner dependent on the angle of attack.

Figure 12 provides a zoomed-in view of the surface patterns outboard of the right alula in the dual-alula configuration. Note that the patterns depicted here are very similar to those observed outboard of the alula for the single alula case.

At $\alpha = 15°$, three features can be distinguished: a separation line attributed to the tip vortex (marked in green), a separation line attributed the separation bubble (marked in cyan), and a separation line originating from the alula root (marked in yellow).

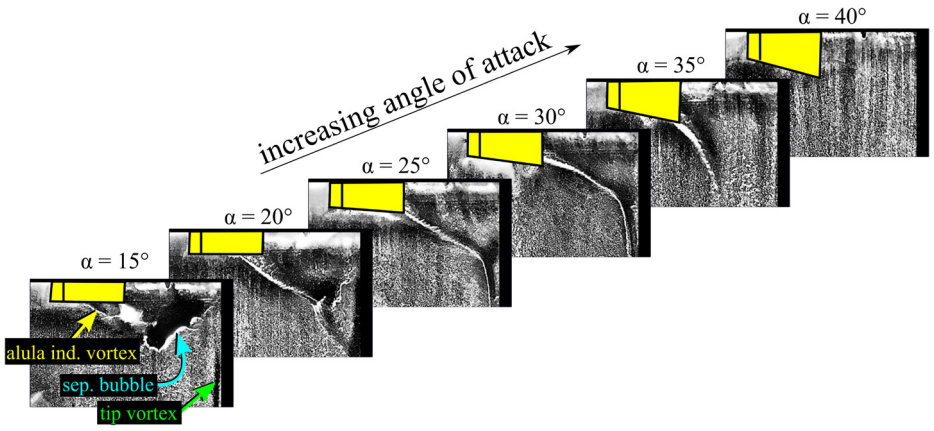

Fig. 12. Effect of angle of attack on the near surface flow structures outboard of the alula. (For interpretation of the colors in the figure(s), the reader is referred to the web version of this article.)

At $\alpha = 20°$, the separation line stemming from the alula root increases in length and sweeps from the root of the alula toward the wing tip. A distinct half-moon shape is observed in the surface patterns obtained at this angle of attack. This feature is likely the consequence of the merging of the alula-induced flow with the separation bubble and the tip vortex. At $25° \leq \alpha < 40°$ the distinct half moon shape is lost and a continuous separation line stems from alula root and sweeps outboard toward the wing tip. At $\alpha = 35°$, the sweeping nature of this separation line is lost as it is observed to tilt in the downstream direction. At $\alpha = 40°$, the separation line stemming from the alula is no longer distinguishable.

The separation line associated with the alula and the accompanying dark 'tracks' that run parallel to it indicate the existence of a discrete vortex. The dark 'tracks' are the result of the initial motion of the carrier fluid. Once the wind tunnel is brought up to speed, these tracks would form as carrier fluid, stemming from the alula root, would sweep across the wing toward the wing tip displacing pigment away from these areas. The motion of the carrier fluid is driven by a combination of shear, pressure, and gravitational forces. The carrier fluid is both drawn toward the low pressure region induced by the vortex on the surface of the wing (which would lie just downstream of the separation line) and drawn downstream on the inclined wing due to gravitational forces. However, the reverse flow of the vortex is impermeable by the carrier fluid causing the carrier fluid to run parallel to the separation lines.

We hypothesize the vortex stemming from the alula's root to be formed when a portion of the leading-edge shear layer confronts the physical barrier of the bottom surface of the alula and is forced to roll-up forming a discrete vortex whose initial orientation is in the spanwise direction. The canted nature of the alula acts as a vortex stabilization mechanism, continually redirecting a component of the freestream flow in the spanwise direction and into the core of the vortex enabling the drainage of vorticity which curtails its detachment. Here, spanwise flow is generated by the canted alula in a similar manner to that of a lifting surface that is inclined to the freestream and at a nonzero roll angle experiences a component of the freestream velocity along its span. Based on the geometry, the magnitude of spanwise flow produced by the alula would tend to increase by $\sin(\alpha)$ enabling the vortex to traverse greater distances over the wing without detachment as angle of attack is increased; a feature consistent with the trends observed in the flow visualizations. The loss of the sweeping separation line at $\alpha = 35°$ and $\alpha = 40°$ is likely a consequence of the vortex lifting off the wing surface at these high angles of attack as suggested by Lee et al. [14].

Hereafter, we will refer to this vortex as the 'sweeping vortex'. We refrain from using the term 'alula vortex' as its vorticity is more likely to stem from the interaction of the wing flow and the alula at the alula's root rather than the shed vorticity of the alula alone. In Section 3.4, we will revisit this claim when we present measurements varying the incidence angle of the alula. We distinguish the current depiction of a sweeping vortex *induced* by the alula of initially spanwise orientation from the depiction of a streamwise vortex *generated* by the alula (recall Fig. 3).

With this interpretation of the surface patterns, we turn our attention back to the load measurements of Fig. 11. The positive roll moment generated at angles of attack in the range $\alpha = 16$–$38°$ for the wing affixed with a single LO alula placed on the left semispan of the wing is consistent with the asymmetric vortex lift produced by the LO alula; specifically its ability to generate and stabilize a vortex that sweeps over the outer portions of the left wing tip. Moreover, the subsequent reduction of roll moment at $\alpha \geq 35°$ is consistent with surface-oil patterns which suggest the reduced interaction of the sweeping vortex with the wing. Accordingly the roll moment measurements in accordance with flow visualizations suggest the roll-moment-generating ability of the alula is tied to the sweeping vortex to which it induces. Despite the roll-moment-generating ability of the alula, global lift enhancement is only observed at poststall angles of attack, $\alpha = 24$–$40°$. At lower angles of attack in the range $\alpha = 16$–$22°$, global lift, drag, and pitching moment is reduced with the addition of either a single alula or dual-alulae. These trends were attributed to the alula's interference with the arch-type vortex harbored by the plain wing.

3.2. Alula spanwise position

The sweeping nature of the vortex induced by the alula observed in flow visualizations further motivates the following investigation of the spanwise position of the alula. We first consider the dual-alula configuration. The geometrical and orientational parameters of the alula are identical to the previous experiment (Fig. 11), i.e. $\phi = 25°$, $\gamma = 20°$ and $l = 0.15b$ ($A_a = 0.011S$), however, now the spanwise location of each alula is varied. In each experiment the alulae are shifted symmetrically such as to maintain a spanwise symmetry of the wing about its midplane.

Figure 13a compares lift, drag, and nose-down pitching moment coefficient curves of the wing with alulae placed at various spanwise locations, $|y/(b/2)|$. The spanwise location of the alulae influences both the magnitude of prestall lift-loss and the magnitude of post-stall lift enhancement.

To assist in interpreting trends in aerodynamic loads with regard to the spanwise location of the alula, Fig. 13b plots the change

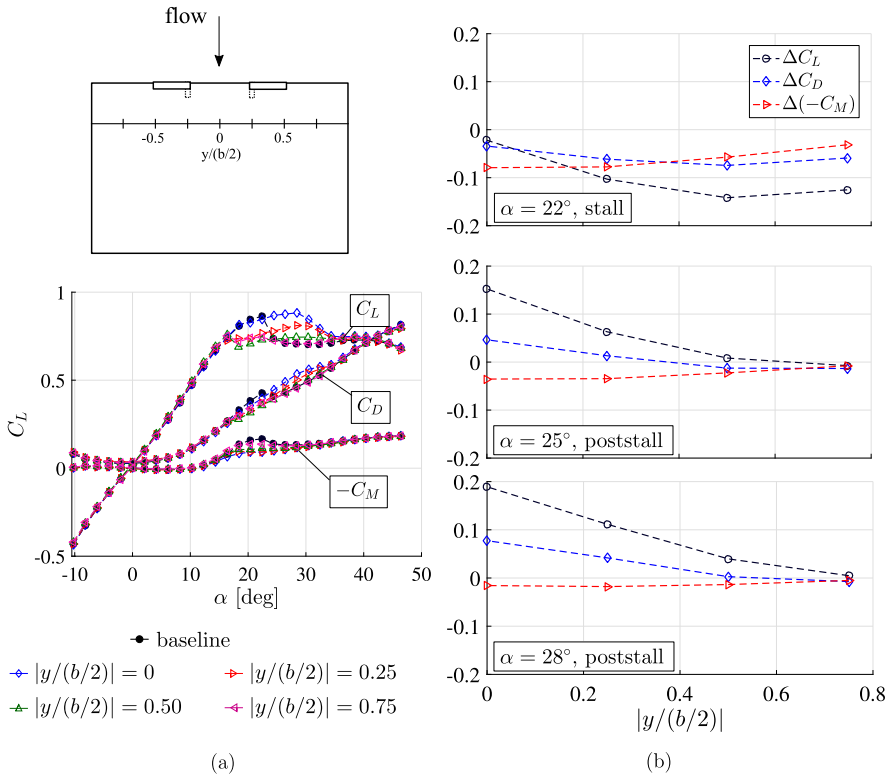

Fig. 13. (a) Lift, drag, and nose-down pitching moment coefficient as a function of angle of attack for dual-opposing alulae placed at various spanwise locations $|y/(b/2)|$. (b) Change in lift, drag, and nose-down pitching moment coefficient relative to baseline wing as a function of the spanwise location of the alulae at select angles of attack.

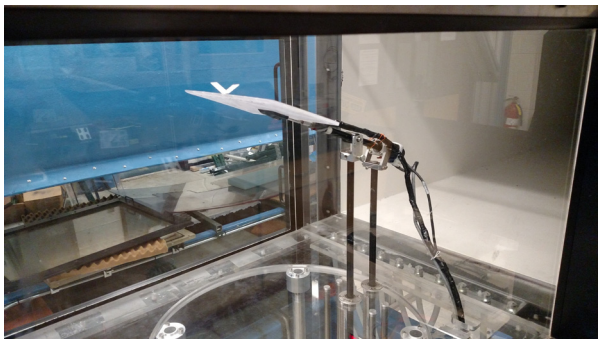

Fig. 14. $\mathcal{R} = 1.5$ wing with dual-opposing alula at $|y/(b/2)| = 0$.

in lift, drag, and nose-down pitching moment coefficient relative to baseline wing as a function of the spanwise location of the alulae at select angles of attack. Here, $\alpha = 22°$ represents the stall angle of attack for the baseline wing, as indicated by $\alpha_{C_{L_{max}}}$, and $\alpha = 25°$ and 28° represent post-stall angles of attack for the baseline wing.

A maximum 25% increase in post-stall lift ($\Delta C_L = 0.19$) relative to the baseline wing occurs at $\alpha = 28°$ when the alulae are centered on the wing in a V configuration, $|y/(b/2)| = 0$ (see Fig. 14). This occurs alongside a 16% increase in drag ($\Delta C_D = 0.08$) and a 11% reduction in nose-down pitching moment ($\Delta C_M = 0.016$). With this configuration, i.e. $|y/(b/2)| = 0$, the adverse effects associated with the alula at prestall angles of attack are minimized, namely the reduction in lift and nose-down pitching moment (see $\alpha = 22°$ in Fig. 13b). Locating the alulae further toward the wing tips (or increasing $|y/(b/2)|$) degrades the performance benefit of the alulae. For example, spacing the alulae away from the midspan of the wing both reduces post-stall lift enhancement and increases pre-stall lift loss over the lift-optimum alula placement, $|y/(b/2)| = 0$.

We turn to surface-oil visualizations to understand the connection between the spanwise location of the alula in this dual-alula configuration and associated aerodynamics. Figure 15 depicts surface patterns obtained on the wing affixed with dual-opposing alulae at $|y/(b/2)| = 0.25$ and $|y/(b/2)| = 0$ compared to the wing with no alula. The angle of attack for each case is $\alpha = 25°$ representing a post-stall angle of attack. We use the inline mounting strategy to enable a more direct comparison with load measurements.

In contrast to the baseline case, the surface patterns for both dual-alulae cases, Fig. 15b and Fig. 15c, reveal two separation lines of which were previously attributed to a sweeping vortex induced by the alula. In comparing Fig. 15b and Fig. 15c, the spanwise position of the alulae appears to control the length of the sweeping vortices induced by the alulae. Notably for the $|y/(b/2)| = 0$ case, Fig. 15c, the sweeping vortex on both sides of the wing extends across each semispan of the wing. The distance of the alula from the wing tip, rather than the distance of the alula from the midspan, appears to be the critical parameter with regard to the spanwise position of the alula. Comparing with the load measurements of Fig. 13b at the same angle of attack ($\alpha = 25°$), increasing the distance of the alula from the wing tip (i.e. decreasing $|y/(b/2)|$), increases the length of the sweeping vortex which increases the control force of the alula.

Next, we consider a single alula configuration in order to interpret its effect on the roll-moment-generating ability of the alula. In these tests, we vary the spanwise position of a LO alula keeping the orientation of the alula fixed at $\phi = 25°$ and $\gamma = 20°$, and the length of the alula at $0.15b$. We now consider the nondimensional distance of the LO alula from the left wing tip, $d/(b/2)$, rather than the distance of the alula from the midspan. For this single alula configuration, the distances tested ranged from $d/(b/2) = 0.25$–1.75.

Fig. 16a compares lift, drag, and nose-down pitching moment coefficient curves and Fig. 16b compares roll moment coefficient

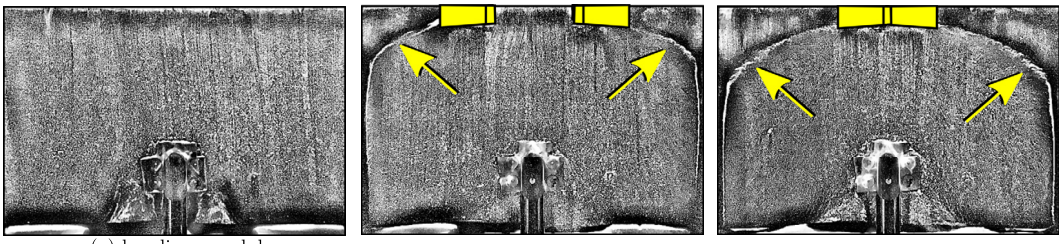

(a) baseline, no alula (b) dual-opposing alula at $|y/(b/2)| = 0.25$ (c) dual-opposing alula at $|y/(b/2)| = 0$

Fig. 15. Surface-oil flow visualizations of an $\mathcal{AR} = 1.5$ wing at $\alpha = 25°$ with (a) no alula and dual-opposing alula whose roots are located at (b) $|y/(b/2)| = 0.25$ and (c) $|y/(b/2)| = 0$, respectively.

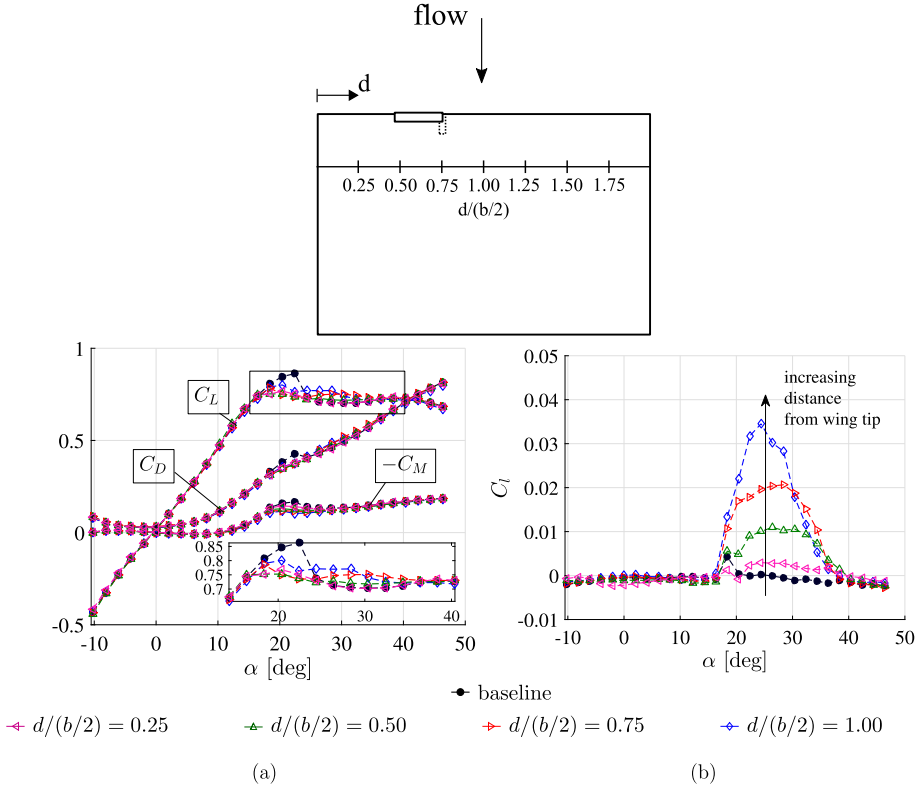

Fig. 16. Effect of the spanwise distance of a single LO alula from the left wing tip on the (a) lift, drag, and nose-down pitching moment coefficient and (b) roll moment coefficient curves of an $\mathcal{AR} = 1.5$ rectangular wing.

curves of the wing with the alula placed at distances from the left wing tip ranging from $d/(b/2) = 0.25$–1.00.

At distances in this range, the wing with a LO alula generates a positive roll moment of magnitude proportional to its distance from the left wing tip. The maximum roll moment occurs with the alula root *centered on the wing*, $y/(b/2) = 0$. This result is counter intuitive if one anticipates the alula to act like a leading-edge control surface where increasing the distance of the control surface from the wingtip decreases its moment arm. The alula is clearly not a conventional lifting surface. The maximum roll moment generated by the alula is $C_l = 0.036$ which occurs at $\alpha \approx 24°$. For comparison, the control force of a $-20°$ flap-aileron deflection on an $\mathcal{AR} = 1.5$ wing at $\alpha = 0°$ is $C_l = 0.033$ (this value was interpolated from the wing data presented in Fig. 1). The miniature alula produces a control force at high angles of attack of greater magnitude than a flap aileron at zero angle of attack. Note that for the reference case, the wetted area of the flap aileron is $A_a \approx 0.12S$, where S is the wing area. For comparison, the wetted area of the alula is $A_a = 0.011S$. The wetted area of the alula is one order of magnitude smaller than that of the flap aileron. While the roll-moment-generating ability of the alula at high angles of attack is intriguing, the downside of the alula is that it does not produce a significant rolling moment at low incidences.

Surface-oil flow visualizations were obtained at $\alpha = 25°$ for the corresponding single alula cases. Figure 17 displays the effect of the LO alula's distance from the left wing tip on surface-oil patterns associated with the alula. Also included are corresponding measurements of the change in lift, drag, nose-down pitching moment, and roll moment coefficient over the baseline wing as a function of alula's distance from the left wing tip.

As the alula is positioned further from the left wing tip at distances ranging from $d/(b/2) = 0.25$ to $d/(b/2) = 1.25$, the vortex that originates from the alula root continues to increase in length sweeping a longer distance across the wing toward the wing tip. From Fig. 17a, the change in lift and drag increases exponentially with increasing distance from the left wing tip where the change in lift reaches a maximum value of 0.09 at $d/(b/2) = 1.25$ which corresponds to a 12.7% increase in lift over the baseline wing at this angle of attack. In contrast, the roll moment increment increases monotonically with increasing distance of the alula from

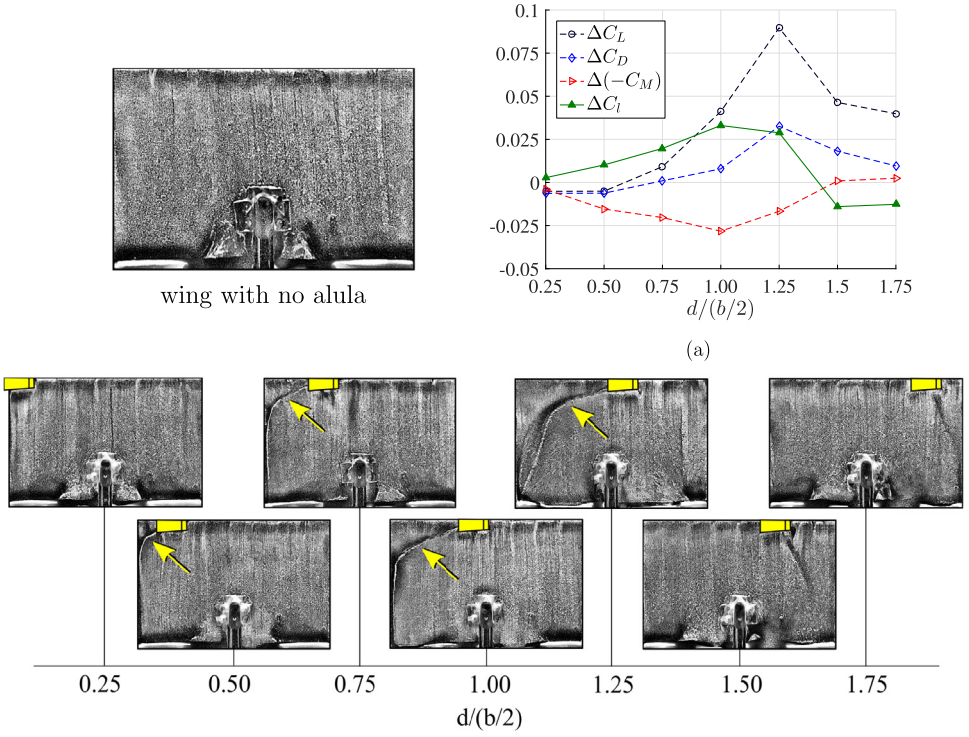

Fig. 17. (a) Effect of the spanwise distance of a single LO alula from the left wing tip on the change in lift, drag, nose-down pitching moment, and roll moment coefficient relative to the plain wing (no alula). $\alpha = 25°$, $C_L \approx 0.734$. Images depict corresponding surface-oil visualizations. Flow is from top to bottom.

the wing tip reaching a peak value at $d/(b/2) = 1.00$. Pitching moment trends follow that of roll moment where a monotonic reduction in nose-down pitching moment occurs with increasing d.

At spanwise locations $d/(b/2) > 1.25$ the sweeping nature of the vortex is lost. Load measurements indicate a net positive increase in lift and drag and roll moment reversal. Dark regions are seen downstream of the alula skewing slightly toward the right wing tip which suggests the presence of the alula-induced vortex there. The existence of this vortex now on the right wing is consistent with the negative roll moment measured for the alula placed at $d/(b/2) > 1.25$.

The surface-oil visualizations in conjunction with load measurements suggest that the lift-optimal spanwise location for the alula occurs at the furthest distance away from the wing tip for which the sweeping nature of the vortex induced by the alula is still retained. Similarly, the maximum roll moment is obtained when the alula is placed at the furthest distance from the wing tip for which the sweeping nature of the alula-induced vortex is still retained unless this distance is greater than the semispan of the wing. For the current case, the maximum roll moment is obtained by placing the alula at the midspan of the wing. It remains unclear whether the loss of the sweeping vortex is the result of distancing the alula too far from the wing tip to which the alula is oriented or the result of the proximity of the alula from the other wing tip. The latter distance would appear to become increasingly important as the aspect ratio of the wing decreases while diminishing in its importance as the wing aspect ratio increases. Due to the intermediate aspect ratio considered, the relative contribution of each of these distances to the loss of the sweeping vortex cannot be distinguished from our experiments.

3.3. Alula span length

We now investigate the effect of the alula geometry. In these experiments we will fix the alula location at the midspan of the wing, $y/(b/2) = 0$, as this spanwise location afforded the largest control force in the operational angle of attack range of the alula for the tested set of alula parameters.

Figure 18 presents lift, drag, nose-down pitching moment, and roll moment coefficient data plotted as a function of angle of attack for the wing with a single LO alula placed at the midspan of the wing, $y/(b/2) = 0$. The alula orientation is the same as the previous experiments, i.e. $\phi = 25°$, $\gamma = 20°$. While previous experiments were conducted with an alula length of $l = 0.15b$, for this experiment, two additional alula lengths were considered: $0.05b$ and $0.10b$. The baseline case represents the plain wing with no alula attachment.

From Fig. 18a, increasing the length of the alula increases lift and drag at post-stall angles of attack while having a minimal effect on the reduction in lift and drag at pre-stall angles of attack. With regard to roll moment, Fig. 18b, the effect of increasing the alula length is to increase the operational angle of attack range of the alula while having a minor influence on the peak magnitude of roll moment. For example, for the smallest alula tested, the operational range of the alula is from $\alpha = 16°$–$28°$ where for the largest tested span length, the operational range of the alula is from $\alpha = 16°$–$38°$.

Based on these measurements, a longer alula would thus be favorable for control purposes in order to increase the operational angle of attack range of the alula. This result provides an explanation for biological trends that depict a correlation between the alula length and both wing loading and wing aspect ratio; namely, the length of the alula tends to increase with increasing wing loading and decreasing wing aspect ratio [15,19]. Both decreasing wing aspect ratio and increasing wing loading (holding airspeed constant), requires a higher angle of attack to trim. Based on our results, the longer alula for these birds may be necessary in order for the alula to function at these higher angles of attack.

3.4. Alula orientation

Experiments were also conducted varying the alula orientation. In these tests, a RO alula was placed at the midspan of the wing,

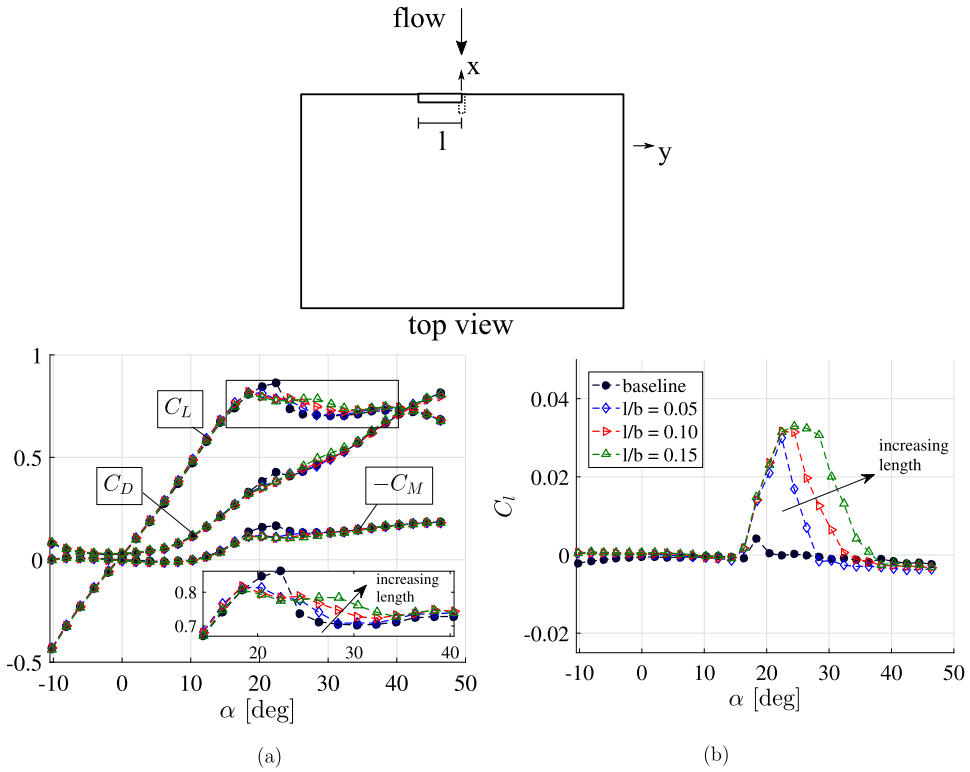

Fig. 18. Effect of alula span length, expressed as the ratio l/b, on the (a) lift, drag, and nose-down pitching moment coefficient and (b) roll moment coefficient curves of an $\mathcal{AR} = 1.5$ rectangular wing.

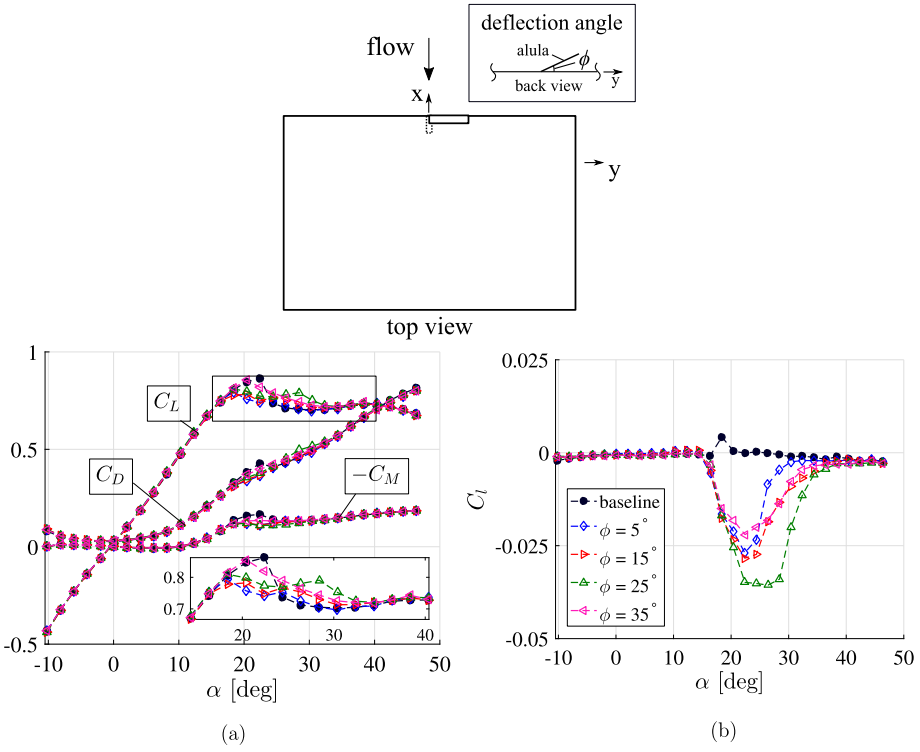

Fig. 19. Effect of alula deflection angle on the (a) lift, drag, and nose-down pitching moment coefficient and (b) roll moment coefficient curves of an $\mathcal{AR} = 1.5$ rectangular wing.

$y/(b/2) = 0$, and the span length and incidence angle of the alula was held at $0.15b$ and $\gamma = 20°$, respectively.

Fig. 19a and Fig. 19b display the effect of alula deflection angle on lift, drag, nose-down pitching moment, and roll moment coefficient curves. In all cases, the RO alula produces a negative roll moment (in contrast to the positive roll moment generated for the LO alula). The magnitude of roll moment is approximately equal and opposite to a LO alula with the same root location.

The dominant effects of the alula deflection angle are two-fold. First, changing the alula deflection angle alters the peak roll moment. The former trend is depicted in Fig. 20 which plots the change in roll moment coefficient as a function of deflection an-

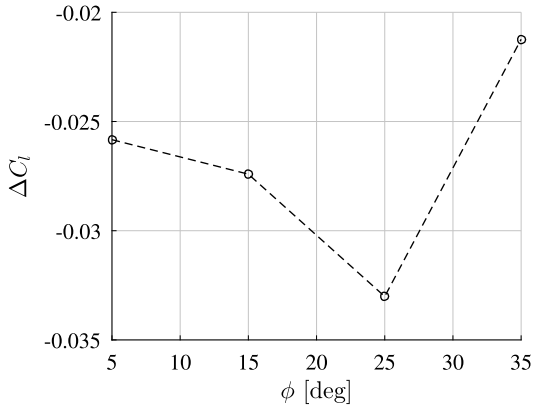

Fig. 20. Change in roll moment coefficient as a function of alula deflection angle at $\alpha = 22°$.

gle ϕ at $\alpha = 22°$. Increasing the deflection angle from $\phi = 5$–$25°$ increases the peak roll moment, although too large of an alula deflection, i.e. $\phi = 35°$, can reduce the peak roll moment.

Second, changing the alula deflection angle in the range $\phi = 5$–$25°$ shifts the upward limit of the operational angle of attack range of the alula, Fig. 19b. For example for $\phi = 5°$ the operational range of the alula is from $\alpha = 16°$–$30°$ where for $\phi = 25°$ the operational range of the alula is from $\alpha = 16°$–$38°$. As was the case for trends with regard to peak rolling moment, too large of an alula deflection, i.e. $\phi = 35°$, can cause the opposite effect and reduce the operational range of the alula.

We now investigate the effect of changing the incidence angle of the alula. If the control forces of the alula were to stem from the aerodynamic lift that it generates then increasing its incidence angle should result in an increase in its control force. Similar trends would be observed if the alula were to act as a vortex generator.

Fig. 21a and Fig. 21b, display the effect of the alula incidence angle on lift, drag, nose-down pitching moment, and roll moment coefficient curves. The deflection angle was held at $\phi = 25°$ and alula root was fixed at the midspan of the wing. Relative to the other parameters considered in this study, the incidence angle has the least influence on the control force produced by the alula. This result suggests that the control force of the alula considered in this study has nothing to due with the lift that it generates. Rather, as was proposed earlier, it is the sweeping vortex induced at the alula's root and subsequently stabilized by the alula which results in the observed control forces. Let us now distinguish the alula, as studied in this manuscript, from traditional high angle of attack devices such as fences, dog-teeth, and vortex generators. Fences and dog-teeth, typically found on swept-winged aircraft, are used to obstruct spanwise flow to prevent boundary layer thickening and ensuing tip stall. For this task, the fence acts as physical barrier to spanwise flow while the dog tooth produces a streamwise vortex that also impedes spanwise flow. Vortex generators also produce streamwise vortices which re-energize the boundary layer to maintain attached-flow conditions over downstream portions of the wing and control surfaces. In contrast with these devices, the alula (in the current investigation) does not prevent or delay stall but rather causes it, if errantly deployed. Moreover, the alula does not generate a vortex but rather induces one, and the canted nature of the alula is such that spanwise flow is most certainly produced rather than stagnated. Lastly, the vortex that it induces is not oriented in the streamwise direction but rather in the spanwise direction, at least initially, until turning downstream at spanwise stations near the wing tip.

4. The sliding alula concept

We have shown that the interaction of the induced sweeping vortex with the wing and the resultant aerodynamic loads can be

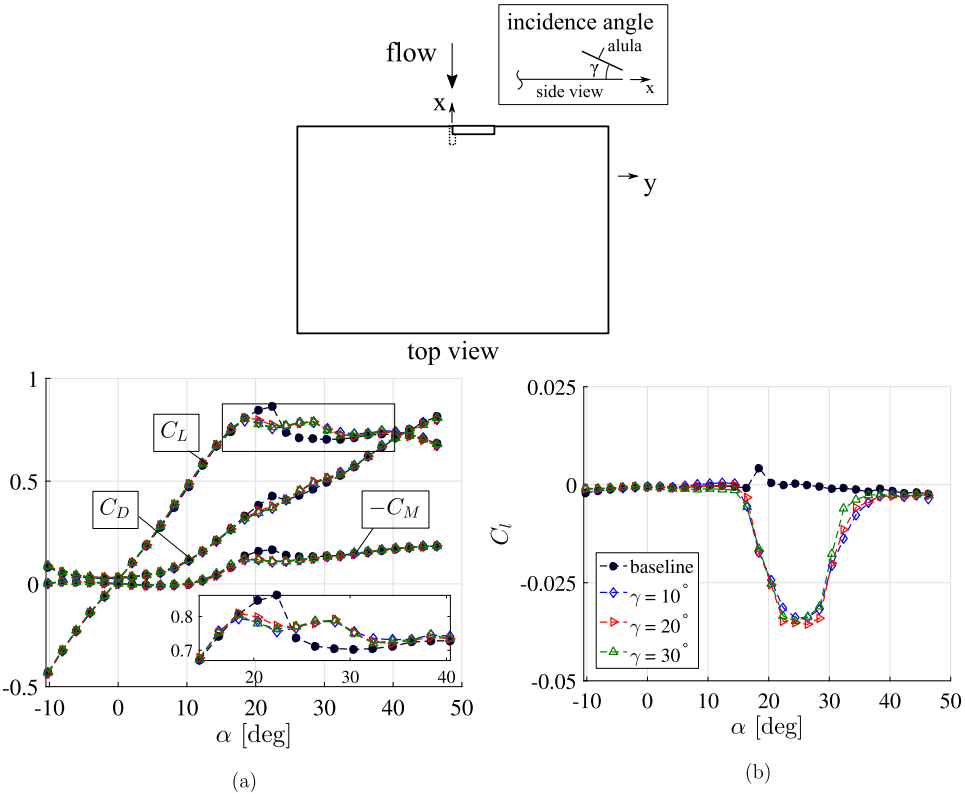

Fig. 21. Effect of alula incidence angle on the (a) lift, drag, and nose-down pitching moment coefficient and (b) roll moment coefficient curves of an $\mathcal{AR} = 1.5$ rectangular wing.

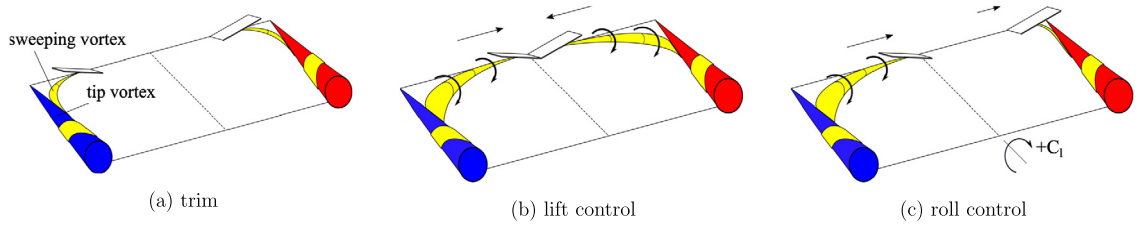

Fig. 22. Schematic of sliding alula control of lift and roll moment at high angles of attack.

controlled, over a wide range of angles of attack, by varying the spanwise position of the alula. This finding motivates a new strategy for lift and roll control of lifting surfaces at high post-stall angles of attack, the sliding alula, which entails coordinated shifting of two deflected alulae along the leading edge of the wing to control i) the total length of sweeping vortices on the wing (lift control) and ii) the asymmetry of the sweeping vortices (roll control).

Fig. 22 depicts schematics of a hypothetical lifting surface with sliding alulae. It is assumed that the lifting surface is trimmed at a post-stall angle of attack within the operational angle of attack range of the alula. At trim, Fig. 22a, the alulae are symmetrically placed at spanwise locations which allow sufficient inboard and outboard travel of the alula. About this trim condition, lift can be controlled by the symmetric inboard/outboard movement of the alula, Fig. 22b. Here, inboard motion of the alula increases lift by increasing the length of the sweeping vortices on wing. The outboard motion of the alula reduces this length reducing lift. The change in lift is proportional to the alula travel although the relationship is fairly nonlinear. A consequence of the sliding alula for lift control is the parallel variation of drag. In the current investigation, the ΔC_D is around $0.5\Delta C_L$ at post-stall angles of attack.

More intriguing than the sliding alula for lift control, is the sliding alula for roll control (see Fig. 22c). To control roll moment, synchronized shifting of the alula to the left (right) on the wing generates a negative (positive) roll moment of magnitude proportional to the shift. For example, shifting the alula to the right extends the length of the sweeping vortex on the left semispan while reducing the length of the sweeping vortex on the right semispan. The resultant vortex lift asymmetry favors a positive roll moment. We note that in this study we have not explicitly tested asymmetric pairs of alula and there exists a potential for adverse interactions that effect the control effectiveness. Further investigation into asymmetric alula pairs is an avenue for future work.

4.1. Control authority of the sliding alula in sideslip

The turbulent environment akin to flight at low altitudes can lead to asymmetric flows over the wing and control surfaces which can elicit undesired rolling moments and potentially degrade the control force of an actuator. The magnitude of rolling moments generated in sideslip by wings of low-aspect-ratio are considerably larger than their higher aspect ratio counterparts [34]. While stabilizing in terms of static stability, the large roll stiffness on low-$\mathcal{AR}$ wings can lead to dynamic stability issues. For instance, the slender inertia and low roll damping of the low-aspect-ratio wing coupled with its high roll stiffness can lead to an unstable dutch-roll mode [22]. Ultimately, low-aspect-ratio aircraft must have sufficient authority to both trim the aircraft (low level control), i.e. reject undesired roll moments, and to maneuver for guidance tasks (high level control). It is thus of interest to assess the roll control authority of the sliding alula on this canonical wing in sideslip.

Experiments toward this end were conducted with a single alula on the $\mathcal{AR} = 1.5$ wing in steady sideslip specifically at sideslip angles of $\beta = 0°$, $\beta = -5°$ and $\beta = -10°$. To assess the ability of the alula to reject undesired roll moments due to sideslip, the wing was first affixed with a leeward-oriented (LEO) alula placed on the leeward semispan of the wing at spanwise stations from $y/(b/2) = 0$ to $y/(b/2) = 0.75$. Next, the wing was affixed with a windward-oriented (WO) alula placed on the windward semispan of the wing at spanwise stations from $y/(b/2) = -0.75$ to $y/(b/2) = 0$ with the goal of assessing the ability of this alula configuration to produce an additional roll moment, atop of that generated due to sideslip, which would be useful for performing extreme maneuvers.

Roll moment measurements for the $\mathcal{AR} = 1.5$ wing are presented in Fig. 23. The roll moment curve for the plain wing in sideslip is assessed first. For each nonzero sideslip angle, roll moment increases with angle of attack until $\alpha = 18°$. In comparing Fig. 23a–c, the magnitude of roll moment coefficient at a given angle of attack is larger for the higher sideslip angle. The following equation accurately captures these trends for low-aspect-ratio wings at low-to-moderate angles of attack:

$$C_l(\alpha) = (C_{l_\beta}/C_L)C_L(\alpha)\beta, \tag{1}$$

where, C_{l_β}/C_L, is the gust sensitivity parameter previously derived for low-$\mathcal{AR}$ straight wings defined by their sweep angle, aspect ratio, and taper ratio in [34]. For rectangular wings $C_{l_\beta}/C_L = -3/(8AR)$. $C_L(\alpha)$ is given analytically for thin, low-aspect-ratio rectangular wings by DeVoria and Mohseni [25] but may also be also obtained via the method of Lamar [35] with little distinction. At $\alpha > 18°$, roll moment stalls and agreement with Eq. (1) is lost as subsequent increases in angle of attack result in the reduction in the magnitude of roll moment. The roll stall trend for the $\mathcal{AR} = 1.5$ wing was previously analyzed via S-DPIV measurements in [11] and was determined to be the result of asymmetric spanwise expansion of stalled flow on the sideslipped wing.

The alula influences roll moments at $\alpha > 16°$ which consists largely of angles of attack in the roll stall regime for the $\mathcal{AR} = 1.5$ wing. The dominant effect of the leeward-oriented (LEO) alula placed on the leeward wing is to reduce the roll moment induced by sideslip by a magnitude proportional to its distance from the leeward wing tip. Importantly, for the LEO alula case there exists a spanwise location of the alula that completely negates the roll moment due to sideslip within the operational angle of attack range of the alula. The opposite effect occurs for the windward-oriented (WO) alula placed on the windward wing where the roll moment is increased by a magnitude proportional to its distance from the windward wing tip. This may be helpful for performing extreme maneuvers.

The control derivative, $(|C_l|)_{|y^*|}$ where $y^* = y/(b/2)$, of the LEO and WO alula was computed at each sideslip angle at $\alpha = 25°$. These values are shown in Table 1. The absolute values are used to indicate how increasing the distance of the alula from the midspan (i.e. $|y^*|$) alters the magnitude of the roll moment increment produced by the alula. The negative values of the control derivatives imply that increasing $|y^*|$ reduces the magnitude of the roll moment increment associated with the alula. Sideslip appears to influence the control derivatives of the alula in an asymmetric

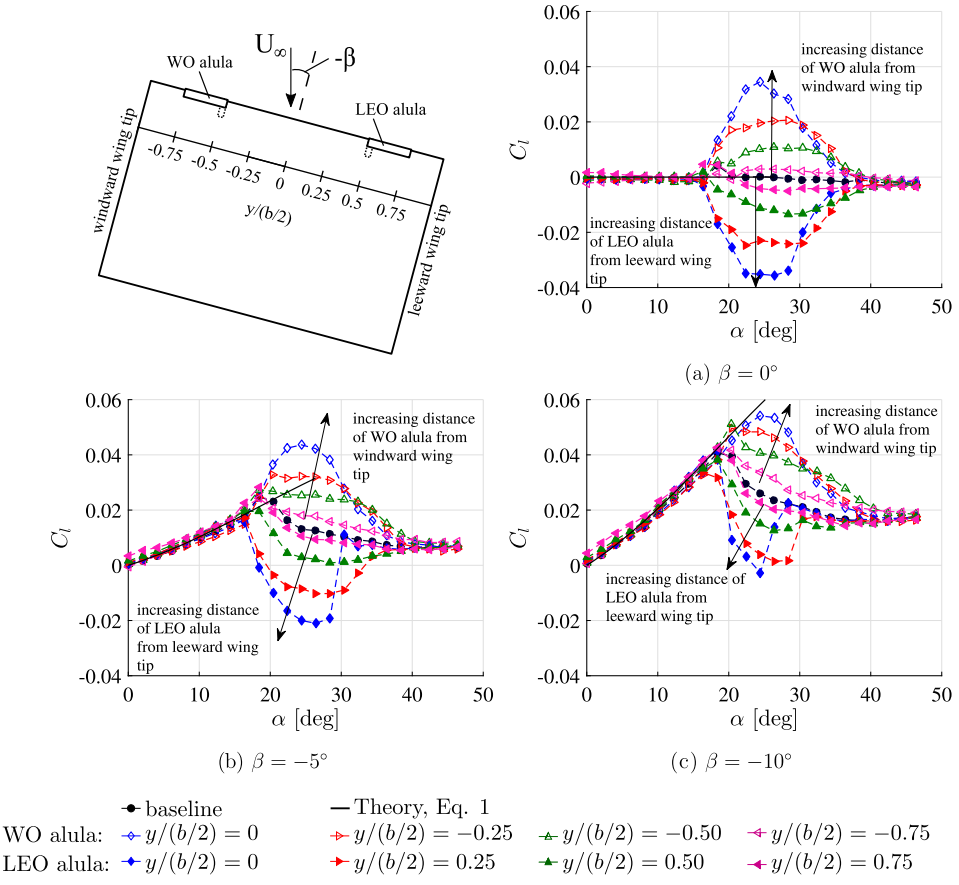

Fig. 23. Roll moment coefficient as a function of angle of attack for the $\mathcal{R} = 1.5$ wing at $\beta = 0°$, $\beta = -5°$, and $\beta = -10°$ equipped with either a leeward-oriented (LO) alula placed on the leeward wing semispan or a windward-oriented (WO) alula placed on the windward wing semispan.

Table 1
Effect of sideslip on the control derivative of a sliding alula, $(|C_l|)_{|y^*|}$. $\alpha = 25°$.

	$\beta = 0°$	$\beta = -5°$	$\beta = -10°$
LEO	−0.0419	−0.0413	−0.0279
WO	−0.0401	−0.0330	−0.0280

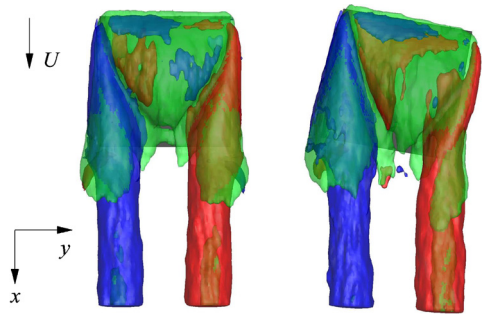

Fig. 24. Mean-flow vortex structure (iso-surfaces) of an $\mathcal{R} = 1$ wing at side-slip angles (left) $\beta = 0$ and (right) $\beta = -10°$. Green: $\omega_z > 0$, red: $\omega_x > 0$, blue: $\omega_x < 0$. From DeVoria & Mohseni. [25].

manner. For example, at $\beta = -5°$ the control derivative of the WO alula is reduced by 18% while the control derivative of the LEO alula is minimally affected. At $\beta = -10°$, a $\approx 30\%$ reduction in the control derivative is evident for both configurations.

The asymmetry in control effectiveness of the WO and LEO alula at low sideslip angles is likely the result of asymmetric vortex flows over thin, low aspect ratio wings in sideslip. This asymmetry is depicted in the schematic in Fig. 24 for an $\mathcal{R} = 1$ wing at $\alpha = 35°$ at $\beta = -10°$. The upstream tip vortex convects over the windward portion of the wing in the streamwise direction while the downstream tip vortex 'hugs' the leeward side edge [25]. The former feature would shorten the length of the sweeping vortex induced by the WO alula on the windward portion of the wing which would reduce its control effectiveness by a magnitude proportional to sideslip angle. Direct measurements of the flow over the wing in the region outboard of the alula are planned to investigate this hypothesis.

4.2. Future work

The experiments presented herein were conducted on a single canonical wing and while the results regarding the sliding alula are enticing they should in no way be interpreted as representative of all wings or lifting surfaces. Additional experiments are required to further mature the sliding alula concept and its applicability to real world applications. Several of such experiments are itemized below:

- testing of asymmetric alula pairs,
- quantitative measurements of the sweeping vortex,
- effect of planform geometry of the baseline wing: aspect ratio and sweep effects,
- effects of turbulence (both intensity and length scales),
- effects of dynamic actuation of the alula,
- sliding alula during flapping (accelerating) flight.

5. Conclusion

A series of wind tunnel experiments were conducted on a flat-plate rectangular $\mathcal{R} = 1.5$ wing affixed with model alulae. The goals were to 1. further our understanding of the physical mecha-

nisms of the alula and 2. identify critical parameters of the alula that influence control forces. This work supplements ongoing research efforts to develop lightweight, minimally intrusive, high-angle-of-attack control technologies to improve low-speed handling qualities of fixed-wing aircraft.

A crucial parameter of the alula is found to be its distance from the wing tip to which it is oriented. Over a distinct range of angles of attack, the control force (both lift and rolling moment) of the alula increases as the alula is located further from this wing tip. When centered on the stalled wing, the single alula generates a rolling moment of magnitude greater than that of a $-20°$ flap-aileron deflection at *zero angle of attack*, where the wetted area of the alula is *an order of magnitude smaller* than that of the reference flap aileron.

Surface-oil visualizations shed light on the underlying aerodynamic mechanisms driving the uncharacteristically large control forces produced by the alula. The interaction of the wing flow and the alula near the alula's root results in a vortex, initially of span-wise orientation, that sweeps across the outer portions of the wing toward the wing tips. The length of this 'sweeping vortex' can be altered by varying the distance of the alula from the wing tip. Varying the incidence angle of alula had negligible effect on control forces; a result that discounts the role of the alula as the vortex generator at least for the wing-alula geometries considered in this investigation.

A new high-angle-of-attack control solution is proposed, the sliding alula, which entails coordinated shifting of two alulae to manipulate the length and asymmetry of stabilized 'sweeping vortices' on stalled wings. Experiments of the sliding alula subject to cross-flow depict a reduction in its control effectiveness, however, it remains to be seen if this result is due to the physics of the alula itself or a consequence of the low-aspect-ratio wing considered.

Conflict of interest statement

The authors declare that there is no conflict of interest regarding the publication of this article.

Acknowledgements

The authors acknowledge the thoughtful suggestions and comments of the anonymous reviewers which greatly improved the quality of the manuscript. The authors also gratefully acknowledge the partial financial support of The Air Force Office of Scientific Research (AFOSR) and the National Science Foundation (NSF).

References

[1] J. Fischel, R.L. Naeseth, J.R. Hagerman, W.M. O'Hare, Effect of Aspect Ratio on The Low-Speed Lateral Control Characteristics of Untapered Low-Aspect-Ratio Wings Equipped with Flap and with Retractable Ailerons, NACA TN 1091, National Advisory Committee for Aeronautics, Langley Aeronautical Lab, Langley Field, VA, USA, 1952.
[2] M. Abdulrahim, Flight dynamics and control of an aircraft with segmented control surfaces, in: 42nd AIAA Aerospace Sciences Meeting and Exhibit, No. 2004-128, Reno, NV, USA, January 5–8, 2004.
[3] T. Hu, Z. Wang, I. Gursul, C. Bowen, Active control of self-induced roll oscillations of a wing using synthetic jet, Int. J. Flow Control 5 (3) (2013) 201–214.
[4] T. Hu, Z. Wang, I. Gursul, Attenuation of self-excited roll oscillations of low-aspect-ratio wings by using acoustic forcing, AIAA J. 52 (4) (2014) 843–854.
[5] A. Panta, A. Mohamed, M. Marino, S. Watkins, A. Fisher, Unconventional control solutions for small fixed wing unmanned aircraft, Prog. Aerosp. Sci. 102 (2018) 122–135.
[6] A.R. Jones, N.M. Bakhtian, H. Babinsky, Low Reynolds number aerodynamics of leading-edge flaps, J. Aircr. 45 (1) (2008) 342–345.
[7] K.J. Drost, H. Johnson, S.V. Apte, J.A. Liburdy, Low Reynolds number flow dynamics of a thin airfoil with an actuated leading edge, in: 41st AIAA Fluid Dynamics Conference and Exhibit, No. 2011-3904, Honolulu, Hawaii, USA, June 27–30, 2011.
[8] C.P. Ford, R. Stevens, H. Babinsky, Flexible leading edge flap on an impulsively started flat plate at low Reynolds number, in: 42nd AIAA Fluid Dynamics Conference and Exhibit, No. 2012-2840, New Orleans, LA, USA, June 25–28, 2012.
[9] A. Panta, P. Petersen, M. Marino, S. Watkins, A. Fisher, A. Mohamed, Qualitative investigation of the dynamics of a leading edge control surfaces for MAV applications, in: IMAV 2017: International Micro Air Vehicle Conference and Competition, Toulouse, France, September 18–21, 2017.
[10] I. Gursul, G. Taylor, C. Wooding, Vortex flows over fixed-wing micro air vehicles, in: 40th AIAA Aerospace Sciences Meeting and Exhibit, No. 2002-0698, Reno, NV, USA, January 14–17, 2002.
[11] T. Linehan, K. Mohseni, Leading-edge flow reattachment and the lateral static stability of low-aspect-ratio rectangular wings, Phys. Rev. Fluids 2 (11) (2017) 23.
[12] R.S. O'Donnell, K. Mohseni, Roll control of low aspect ratio wings using articulated winglet control surfaces, J. Aircr. (2019), https://doi.org/10.2514/1.C034704, in press.
[13] T. Hu, Z. Wang, I. Gursul, Passive control of roll oscillations of low-aspect-ratio wings using bleed, Exp. Fluids 55 (6) (2014) 1752.
[14] S. Lee, J. Kim, H. Park, P.G. Jabłoński, H. Choi, The function of the alula in avian flight, Sci. Rep. 5 (9914) (2015) 63–68.
[15] J.C. Alvarez, J. Meseguer, A. Perez, E. Meseguer, On the role of the alula in the steady flight of birds, Ardeola 48 (2) (2001) 161–173.
[16] J.J. Videler, Avian Flight, Oxford University Press, Oxford, NY, USA, 2003.
[17] A.C. Carruthers, A.L.R. Thomas, G.K. Taylor, Automatic aeroelastic devices in the wings of a steppe eagle Aquila nipalensis, J. Exp. Biol. 210 (2007) 4136–4149.
[18] B. Austin, A.M. Anderson, The alula and its aerodynamic effect on avian flight, in: Proceedings of the ASME International Mechanical Engineering Congress and Exposition, No. IMECE2007-41693, Seattle, Washington, USA, November 11–15, 2007, pp. 797–806.
[19] S. Lee, H. Choi, Characteristics of the alula in relation to wing and body size in the Laridae and Sternidae, Anim. Cells Syst. 21 (1) (2017) 63–69.
[20] J. Meseguer, S. Franchini, I. Prez-Grande, J.L. Sanz, On the aerodynamics of leading-edge high-lift devices of avian wings, Proc. Inst. Mech. Eng., Part G, J. Aerosp. Eng. 219 (1) (2005) 63–68.
[21] B.A. Mandadzhiev, M.K. Lynch, L.P. Chamorro, A.A. Wissa, An experimental study of an airfoil with a bio-inspired leading edge device at high angles of attack, Smart Mater. Struct. 26 (9) (2017) 094008.
[22] M. Shields, K. Mohseni, Inherent stability modes of low aspect ratio wings, J. Aircr. 52 (1) (2015) 141–155.
[23] M. Shields, K. Mohseni, Roll stall for low-aspect-ratio wings, J. Aircr. 50 (4) (2013) 1060–1069; J. Aircr. 53 (4) (2016) 1186–1188 (Erratum).
[24] M. Shields, K. Mohseni, Passive mitigation of roll stall for low aspect ratio wings, Adv. Robot. 27 (9) (2013) 667–681.
[25] A.C. DeVoria, K. Mohseni, A vortex model for forces and moments on low-aspect-ratio wings in side-slip with experimental validation, Proc. R. Soc. A 473 (2198) (2017).
[26] R.S. O'Donnell, K. Mohseni, Aerodynamic parameter estimation from wind tunnel testing of a small UAS, in: Proceedings of the AIAA Atmospheric Flight Mechanics Conference, No. 2018-0066, Kissimmee, Florida, USA, January 8–12, 2018.
[27] T. Linehan, M. Shields, K. Mohseni, Development, characterization, and validation of a four axis wind tunnel positioning system, in: Proceedings of the AIAA Aerospace Sciences Meeting, No. 2014-1308, National Harbor, MD, USA, January 13–17, 2014.
[28] W.H. Rae, A. Pope, Low-Speed Wind Tunnel Testing, 3rd ed., John Wiley and Sons, New York City, NY, USA, 1999.
[29] H.W. Coleman, W.G. Steele, Experimentation, Validation, and Uncertainty Analysis for Engineers, 3rd ed., John Wiley and Sons, Hoboken, NJ, USA, 2009.
[30] M. Mizoguchi, H. Itoh, Effect of aspect ratio on aerodynamic characteristics at low Reynolds numbers, AIAA J. 51 (7) (2013) 1631–1639.
[31] M.R. Visbal, T.O. Yilmaz, D. Rockwell, Three-dimensional vortex formation on a heaving low-aspect-ratio wing: computations and experiments, J. Fluids Struct. 38 (2013) 58–76.
[32] M.R. Visbal, Three-dimensional flow structure on a headving low-aspect-ratio wing, in: Proceedings of the 49th AIAA Aerospace Sciences Meeting, No. 2011-219, Orlando, FL, USA, January 4–7, 2011, pp. 1–24.
[33] M.R. Visbal, Unsteady flow structure and loading of a pitching low-aspect-ratio wing, Phys. Rev. Fluids 2 (2017) 024703.
[34] T. Linehan, K. Mohseni, Theoretical prediction of roll moment due to sideslip for thin low-aspect-ratio wings, AIAA J. (2019), in press.
[35] J.E. Lamar, Extension of Leading-Edge Suction Analogy to Wings with Separated Flow Around the Side Edges at Subsonic Speeds, Technical Report TR R-428, NASA, Langley Research Center, Hampton, VA, USA, July 1974.